Investigation on Third-Order Intermodulation Distortions Due to Material Nonlinearities in TC-SAW Devices

Vikrant Chauhan, *Student Member, IEEE*, Markus Mayer, *Member, IEEE*, Elena Mayer, Werner Ruile, Thomas Ebner, Ingo Bleyl, *Member, IEEE*, Karl C. Wagner, *Member, IEEE*, Robert Weigel, *Fellow, IEEE*, Andreas P. Mayer, *Member, IEEE*, and Amelie Hagelauer, *Member, IEEE*

***Abstract*— Nonlinearity can give rise to intermodulation distortions in surface acoustic wave (SAW) devices operating at high input power levels. To understand such undesired effects, a finite element method (FEM) simulation model in combination with a perturbation theory is applied to find out the role of different materials and higher order nonlinear tensor data for the nonlinearities in such acoustic devices. At high power, the SAW devices containing metal, piezoelectric substrate, and temperature compensating (TC) layers are subject to complicated geometrical, material, and other nonlinearities. In this paper, third-order nonlinearities in TC-SAW devices are investigated. The materials used are $LiNbO_3$-rot128YX as the substrate and copper electrodes covered with a SiO_2 film as the TC layer. An effective nonlinearity constant for a given system is determined by comparison of nonlinear P-matrix simulations to third-order intermodulation measurements of test filters in a first step. By employing these constants from different systems, i.e., different metallization ratios, in nonlinear periodic P-matrix simulations, a direct comparison to nonlinear periodic FEM-simulations yields scaling factors for the materials used. Thus, the contribution of the different materials to the nonlinear behavior of TC-SAW devices is obtained and the role of metal electrodes, substrate, and TC film are discussed in detail.**

***Index Terms*— Geometrical and material nonlinearity, temperature compensated surface acoustic wave (SAW), third-order intermodulation products.**

I. Introduction

LINEARITY is an important issue in high-frequency surface acoustic wave (SAW) and bulk acoustic wave devices for telecommunications systems. Although nonlinearities in SAW devices are very small, they generate third-order intermodulation (IMD3) products, which lead to noticeable signal distortions. This problem even becomes more pronounced with carrier aggregation because several strong signals are present in this case.

A simulation model of nonlinear effects in SAW components is required in order to better characterize, model, and minimize the nonlinearities. The generation of IMD3 caused by the nonlinearity of SAW devices has been studied by several authors based on simplified models such as P-matrix [3], [4], coupling of modes [5], [6], or the Mason model [7], and more recently a model based on the finite element method (FEM) [1], [2], [8]. Fig. 1 gives the overview of the approach to determine the role of material in the generation of IMD3 in SAW devices.

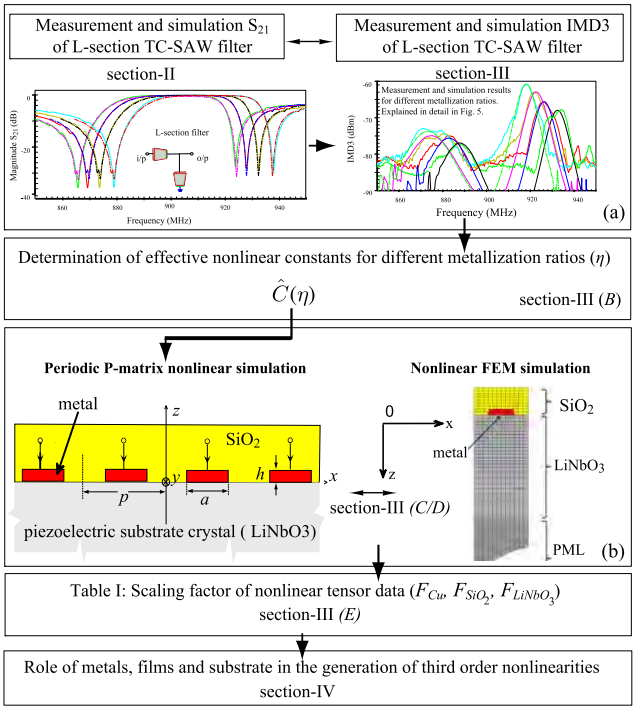

Fig. 1. Overview of the approach to determine the role of material in the generation of IMD3 in SAW devices. (a) As a first step, the linear transfer function of the filter is compared with measurement, and then, the effective nonlinear constant, $\hat{C}(\eta)$ from the P-matrix model is calculated by comparing with IMD3 measurements. $\hat{C}(\eta)$ is used in periodic nonlinear P-matrix model. (b) Results from nonlinear FEM model are compared with periodic nonlinear P-matrix model to determine the scaling factors of nonlinear tensor data of Cu and SiO_2.

Manuscript received November 8, 2017; accepted April 5, 2018. Date of publication May 2, 2018; date of current version October 3, 2018. This work was supported in part by the German Research Foundation in the framework of the MUSIK (MUltiphysical Synthesis and Integration of Complex RF circuits) research group (FOR1522). *(Corresponding author: Vikrant Chauhan.)*

V. Chauhan, R. Weigel, and A. Hagelauer are with the Institute for Electronics Engineering, Friedrich Alexander University Erlangen–Nuremberg, 91058 Erlangen, Germany (e-mail: vikrant.chauhan@fau.de).

M. Mayer, W. Ruile, T. Ebner, I. Bleyl, and K. C. Wagner are with RF360 Europe GmbH, a Qualcomm−TDK Joint Venture, 81671 Munich, Germany (e-mail: markus.mayer@rf360jv.com).

E. Mayer and A. P. Mayer are with the HS Offenburg University of Applied Science, 77723 Offenburg, Germany (e-mail: andreas.mayer@hs-offenburg.de).

Digital Object Identifier 10.1109/TUFFC.2018.2832283

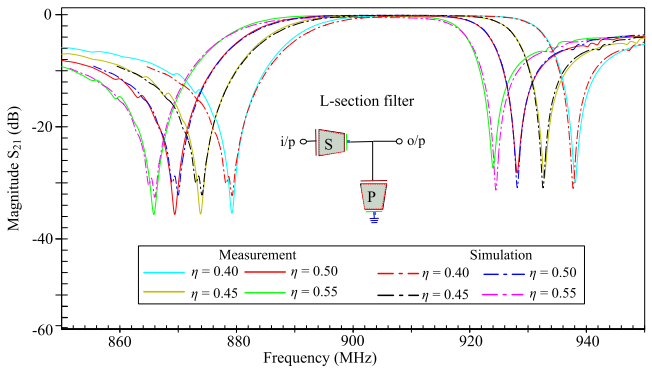

Fig. 2. Measured and simulated S_{21} curves of an L-section SAW filter for different metallization ratios η.

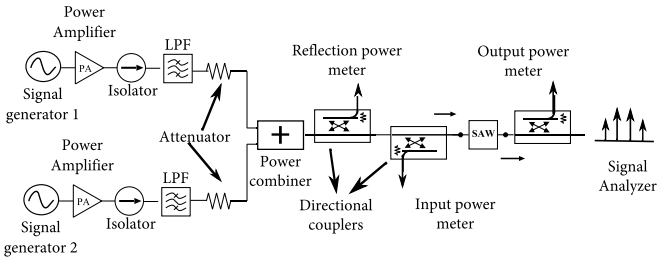

Fig. 3. Schematic of a typical one-port/two-port intermodulation measurement setup for SAW devices.

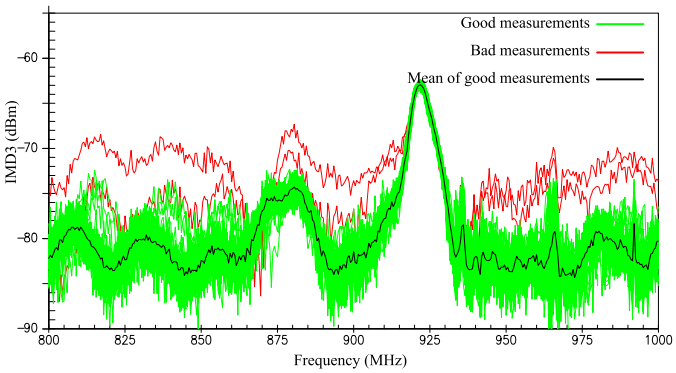

Fig. 4. Wafer measurements of L-section SAW filter for metallization ratio $\eta = 0.50$. The black curve is the mean of good measurements, while the bad measurements are mainly due to probe contact issue.

Nakagawa *et al.* [9] investigated the influence of metal electrodes on the third-order nonlinearity of SAW in lithium tantalate ($LiTaO_3$) devices and explained that the electrode fingers in an interdigital transducer are one of the major sources of the third-order nonlinearity because nonlinear signal levels change markedly depending on the crystallinity of Al. The crystallinity is an important factor that significantly affects the power durability. Good crystallinity leads to longer lifetime. Therefore, to retain the metal electrode crystallinity, Nakagawa *et al.* [9] introduced a titanium (Ti) layer underneath the Al layer in order to reduce the acoustic strain generated by the SAW in the Al layer [17]. It should be noted that the material and wave polarization used in [9] and [17] are different from our investigation.

Using the electroelasticity theory, it was shown that a nonlinear P-matrix simulation model using a single frequency-independent effective nonlinearity constant $\hat{C}(\eta)$, which may depend on the metallization ratio (η), can predict the IMD3 of a layered system very well [3], [5], [8]. In [2] and [8], this very same effective nonlinear constant was theoretically evaluated using a FEM approach, where linear fields, associated with input tones, are combined with the nonlinear material tensor data to obtain the sources of nonlinear fields.

In this paper, the effective approach to calculate the nonlinearities in the SAW devices that fit to experimental data is discussed in detail along with the origin of IMD3. The role of higher order nonlinear material constants of SiO_2, Cu, and $LiNbO_3$ is discussed. Moreover, the introduction of third- and fourth-order nonlinear material tensor data from the literature and of scaling factors can help to achieve the goal of this paper to study the influence of substrate, metal electrodes, and covering layer to the overall nonlinearity in more detail.

II. Measurement Setup and Linear Results

In Section II, the linear S-parameter (S_{21}) results of the SAW filter are discussed and the IMD3 measurement setup is explained.

A. Linear Characteristics

Fig. 2 shows the excellent agreement between the simulations and measurement results of the linear filter transfer function (S_{21}) for different metallization ratios. Since the agreement between measured and simulation results is excellent, we can rely on the calculated linear fields that are the basis of our nonlinear calculations explained in Section III. The test devices used in our calculation are basic L-section SAW filters with one resonator in series and one in parallel as shown in the inset of Fig. 2. The pitch is around 2 μm and different metallization ratios of $\eta = 0.40$, 0.45, 0.50, and 0.55 are considered. The Cu electrode height is 285 nm and the SiO_2 layer has a thickness of h_{SiO_2} = 1376 nm.

The wafer is $LiNbO_3$-rot 128YX with an unpolished backside. Since we perform on-wafers measurements, only the electrical connection, but no package has to be considered in the simulation.

B. IMD3 Measurement Setup

The experimental setup for the wafer measurement of IMD3 for SAW filters is shown in Fig. 3. Two RF signal generators (SGs) are used to generate the two input signals. The amplified main signal tone at 9 dBm sweeping over frequencies 770–1070 MHz is obtained using a power amplifier (PA). The defined frequency spacing Δf between the two input signals is 2 MHz. Each tone signal passes through the isolator, and then, it is combined at the combiner. Low-pass filters are used to suppress the nonlinear signals coming from the SG and PA.

Fig. 4 shows about 40 IMD3 measurements of L-sections with a metallization ratio of $\eta = 0.50$ evenly distributed over the whole wafer, as an example. Ripples due to longitudinal bulk waves [19] might be present but are presumably suppressed by the unpolished wafer backside and the smoothing by calculating the mean value, where failed

measurements have been neglected. The same measurements have been performed with all the other metallization ratios, and in the following, only the mean value evaluated as explained earlier will be considered.

III. Full Nonlinear Simulation Model

Section III explains a three-step approach in the simulation model to calculate the IMD3. Fig. 1(a) shows the linear filter function that is used as a basis for calculating the nonlinear fields. We finally fit the nonlinear P-matrix simulations to experimental data with effective nonlinearity constants, $\hat{C}(\eta)$. These are used in the next step to calculate the IMD3 power in a nonlinear periodic P-matrix simulation. In the last step, this simulation is used as a reference to which the nonlinear periodic FEM calculation is fit. This is done by scaling the nonlinear material constants in nonlinear periodic FEM calculations. Thus, the role of the corresponding materials is highlighted. In Section IV, we discuss the origin of IMD3 and the obtained results.

A. Nonlinear P-Matrix Simulation Model

We consider the case of IMD3 at $2f_1 - f_2$ for two tones applied at f_1 and f_2. The nonlinear P-matrix equation at $2f_1 - f_2$ can be written by extending the linear P-matrix by acoustic and electric nonlinear source terms [3], [4]

$$\begin{pmatrix} b_1 \\ b_2 \\ \mathbf{i} \end{pmatrix} = \begin{bmatrix} \mathbf{P}_{11} & \mathbf{P}_{12} & \mathbf{E}_1 \\ \mathbf{P}_{12}^T & \mathbf{P}_{22} & \mathbf{E}_2 \\ -2\mathbf{E}_1^T & -2\mathbf{E}_2^T & \mathbf{Y} \end{bmatrix} \begin{pmatrix} a_1 \\ a_2 \\ \mathbf{u} \end{pmatrix} + \begin{pmatrix} s_1 \\ s_2 \\ \mathbf{s}_u \end{pmatrix} \quad (1)$$

where $a_{1/2}$ and $b_{1/2}$ are the amplitudes of acoustic waves entering and leaving, respectively, at the left and right ports. $s_{1/2}$ are the nonlinear acoustic sources emitting to the left and right ports and $\mathbf{s}_u$ are the electric current sources. s_1 and s_2 as referenced in [3], can be related to $\hat{C}(\eta)$ as

$$s_1 = \hat{C}(\eta) \cdot \left(b_1^{(1)}\right)^2 \cdot \left(b_1^{(2)}\right)^* \quad (2)$$

and

$$s_2 = \hat{C}(\eta) \cdot \left(b_2^{(1)}\right)^2 \cdot \left(b_2^{(2)}\right)^*. \quad (3)$$

For finite tracks, the nonlinear P-matrixes in (1) are cascaded, thus calculating the series and parallel resonators of an L-section filter. The single nonlinear constant used in our P-matrix simulation should be regarded as an effective constant including all the nonlinear effects [3], [4]. This is only justified by the good agreement between measurement and simulation in the frequency range we considered here. The acoustic sources are determined from the linear acoustic fields at the input tones f_1, f_2 and a single frequency-independent nonlinearity constant, $\hat{C}(\eta)$ [3], [4].

B. Fitting of Nonlinear P-Matrix Simulation to Measurement

The measurement results of IMD3 obtained for the L-section filters are now compared to the nonlinear P-matrix simulations [3] to determine the values of the effective nonlinearity constant $\hat{C}(\eta)$, for the different metallization ratios [$\eta = (a/p)$, a is aperture and p is pitch] as mentioned in Table I. The good agreement between simulation and measurement of L-section filters (series resonator S at the input port and the parallel resonator P) for the different metallization ratios η is shown in Fig. 5. The IMD3 of the series resonator is generated at the antiresonance frequency. Interestingly, the calculated IMD3 power, mainly due to the resonator P, is around three times less dependent on η compared to the IMD3 power computed in transmission mainly due to the series resonator S.

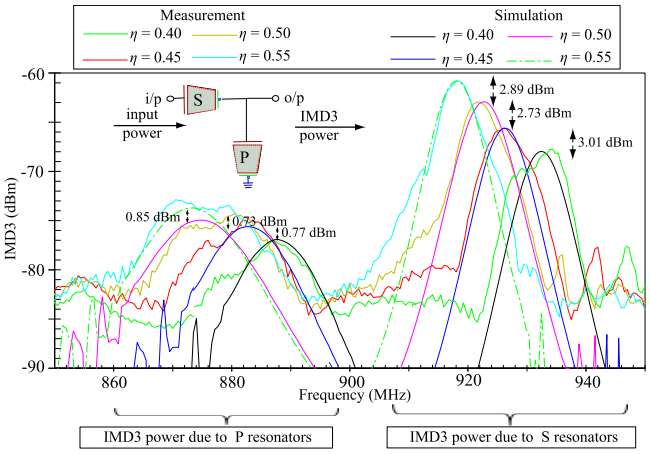

Fig. 5. Measured and simulated IMD3 curves for an incident power of 9 dBm for different metallization ratios η.

TABLE I
CALCULATED EFFECTIVE NONLINEAR CONSTANT $\hat{C}(\eta)$

Metallization ratio (η)	Effective nonlinear constant $\hat{C}(\eta)$ ($W^{-1}GHz^{-2}$)
0.40	0.0051
0.45	0.0076
0.50	0.0097
0.55	0.0112

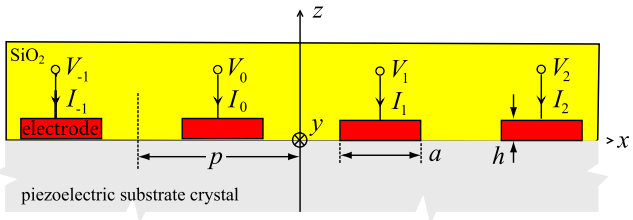

Fig. 6. Periodic array of Cu electrodes on $LiNbO_3$-rot128YX covered with SiO_2. A drive voltage V_n connected over the bus bars of the device excites waves. In reverse, the waves propagating under the electrodes cause flow of the current I_n. The metallization ratio η is (a/p), where p is the pitch and a is the width of electrode.

C. Periodic P-Matrix Simulation Model

To close the gap between the nonlinear P-matrix simulation of a finite resonator and the nonlinear periodic FEM simulation [2], a nonlinear periodic P-matrix model for an infinite periodic system is introduced. We consider a cell with a single electrode and apply the condition of periodicity with a phase shift of π (see Fig. 6). This condition also requires $b_1 = -a_2$

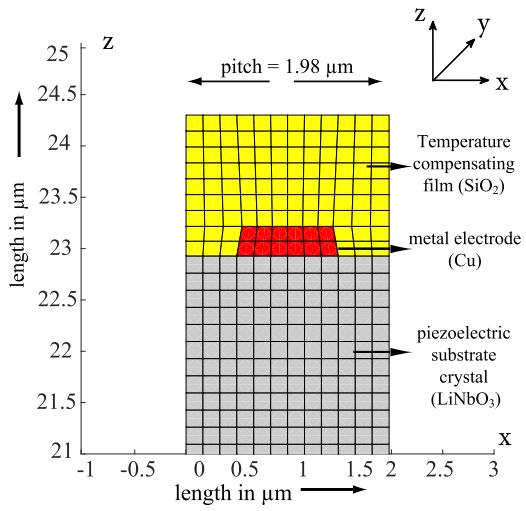

Fig. 7. Unit cell for FEM calculations showing a semi-infinite piezoelectric substrate that is covered by an infinite periodic set of electrodes (Cu) and by an additional film (SiO_2). The nonlinear FEM model is 2-D since variations of the fields along the direction of the electrodes (y-direction) are neglected.

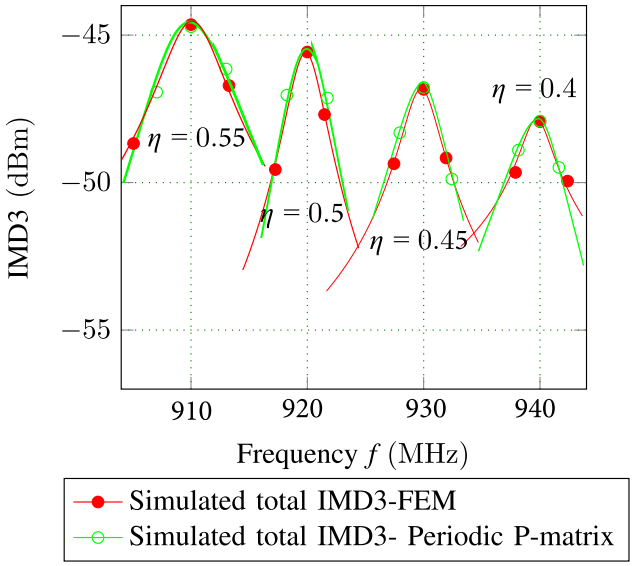

Fig. 8. Comparison of IMD3 between the periodic P-Matrix and periodic FEM simulations of a single resonator at antiresonance for different metallization ratios (η).

and $b_2 = -a_1$ for the linear and nonlinear P-matrix equations. This periodic unit cell of single resonator together with the $\hat{C}(\eta)$ as outlined earlier allows for a direct comparison with the nonlinear periodic FEM simulation model.

D. Periodic Nonlinear FEM Simulation Model

The system considered in the nonlinear finite element model consists of an infinite periodic array of Cu electrodes on the substrate 128° rotated Y-cut of $LiNbO_3$ with Euler angles defined as: $\lambda = 0.0$, $\mu = 37.85°$, and $\theta = 0.0$. The electrodes are embedded in a SiO_2 film as shown in Fig. 7. It consists of one cell of length $p = 1.98$ μm with periodic boundary conditions for the boundaries along the x-axis and a perfectly matched layer below the lower boundary of the substrate in order to avoid reflections (not shown). The SiO_2 layer is assumed to be flat at the top. The nonlinear FEM simulation model is discussed in detail in [2] and [8].

E. Higher Order Nonlinear Material Constants

Throughout this paper, we use the term "nth-order tensor data" to denote the coefficients of the nth-order terms in the expansion of the Gibbs free energy in powers of the Lagrange strain tensor and material frame electric field components. In addition, the term "nonlinear tensor data" is used for the coefficients of the third and higher order terms. "Material nonlinearity" pertains to nonlinear effects associated with the terms in this expansion which are of higher than second order. The expansion coefficients in these terms are the nonlinear material constants.

F. Comparison of Periodic P-Matrix and Nonlinear FEM

In order to match the results from the nonlinear periodic P-matrix simulation, the nonlinear tensor data in the nonlinear FEM simulation were scaled. The third-order tensor data of the substrate are known from the literature and were left unchanged [10], [18]. The fourth-order tensor data of $LiNbO_3$ are unknown to us, and we have set them to zero in all our calculations. The third- and fourth-order nonlinear elastic constants of Cu [12], [13] and SiO_2 [14], [15], respectively, were taken from the literature. Scaling factors (F_{Cu}, $F_{\mathrm{SiO_2}}$, and $F_{\mathrm{LiNbO_3}}$) are the numbers that scale, or multiply, the third- and fourth-order nonlinear material constants. For example, in (4), F_{Cu} is the scale factor for the third-order elastic constants for bulk material of copper ($\mathrm{Cu}_{ijk}^{(\mathrm{bu})}$). F_{Cu} is also the coefficient of ($\mathrm{Cu}_{ijk}^{(\mathrm{bu})}$), and may be called the constant of proportionality of $\mathrm{Cu}_{ijk}^{(\mathrm{up})}$ to F_{Cu}. $\mathrm{Cu}_{ijk}^{(\mathrm{up})}$ is the updated third-order elastic constant of copper (i, j, and k are the Voigt indexes)

$$\mathrm{Cu}_{ijk}^{(\mathrm{up})} = F_{\mathrm{Cu}} \cdot \left(\mathrm{Cu}_{ijk}^{(\mathrm{bu})}\right). \tag{4}$$

Only Cu and SiO_2 scaling factors were fit in order to match the IMD3 power to the results from the nonlinear periodic P-matrix simulation. Fig. 8 shows the result of the fitting achieved with the scaling factors listed in Table II for different metallization ratios η.

TABLE II
SCALING FACTORS OF NONLINEAR TENSOR DATA

Copper metal F_{Cu}	SiO_2 film F_{SiO_2}	$LiNbO_3$ substrate F_{LiNbO_3}
12	3	1

IV. DISCUSSION OF ORIGIN OF IMD3

A. Scaling Factors of Nonlinear Tensor Data

The scaling factors for SiO_2 ($F_{\mathrm{SiO_2}}$) and especially for Cu (F_{Cu}) lead to values of the nonlinear elastic constants that are much larger than the corresponding data for bulk material given in the literature [12]–[15]. The physical origin of this

large discrepancy is still an open question. However, we have to keep in mind that the literature data do not correspond very well to the material of the electrodes or temperature compensating (TC) film in our test devices. For example, the third- and fourth-order elastic constants for Cu used in our FEM calculations, taken from [13], were determined by *ab initio* electronic structure calculations for ideal crystals without defects.

The nonlinear data for the substrate remain unchanged, which might be too simple because the material might have changed in the substrate used for our measurements due to suppression of pyroelectricity. Other types of nonlinearity that cannot be captured by the nonlinear tensor data have been considered negligible. Also, one scaling factor for all nonlinear coefficients is clearly an oversimplification, and much more nonlinear information from measurements would be needed to fit all nonlinear constants individually.

Nevertheless, a very good agreement between simulation and the measured η-dependence could be achieved (see Fig. 8) with the help of only two scaling factors, and therefore, an estimation of the role of the different materials was feasible. Note that if all the scaling factors (F_{Cu}, $F_{\mathrm{SiO_2}}$, and $F_{\mathrm{LiNbO_3}}$) are set to zero, i.e., the "material nonlinearity" vanishes and the "geometrical nonlinearity" is still present.

B. Geometric and Material Nonlinearities

In the following, we distinguish between the geometrical and material nonlinearities. The term "geometrical nonlinearity" is used here with a generalized meaning, denoting those nonlinear effects that result from the second-order terms in the expansion of the Gibbs free energy per unit volume of the undeformed media in powers of the Lagrange strain tensor and the material frame electric field components [11].

A good agreement of IMD3 power for different η between the nonlinear FEM and periodic P-matrix is obtained as already shown in Fig. 8. Therefore, the optimized scaling factors used in the FEM simulation can help to study the role of individual or combination of layers in the generation of IMD3.

In Fig. 9, the role of Cu nonlinearity (third- and fourth-order elastic constants) is evaluated while considering nonlinearities of the other materials ($F_{\mathrm{SiO_2}}$ and $F_{\mathrm{LiNbO_3}}$) as zero. Similarly, the individual role of nonlinearity in SiO_2 (third- and fourth-order elastic constants) and $LiNbO_3$ (third-order elastic, dielectric, piezoelectric, and electrostriction constants) is determined and shown in Fig. 9. Note that the geometric nonlinearity is always present.

The geometric nonlinearity is stronger than the $LiNbO_3$ nonlinearity. This indicates that a strong compensation of geometric and material nonlinearities might occur. For example, in the linear combination of the elastic constants $c_{111} + 3c_{11}$ [2] that determines the growth of the second harmonics of longitudinal bulk waves, c_{111} and c_{11} have opposite signs in most cases. Here, c_{11} and c_{111} are second- and third-order elastic constants, respectively.

Surprisingly, in Fig. 9, the individual nonlinearity of Cu metal is stronger than the total IMD3. This may be due to a partial phase cancellation of the nonlinear contributions of

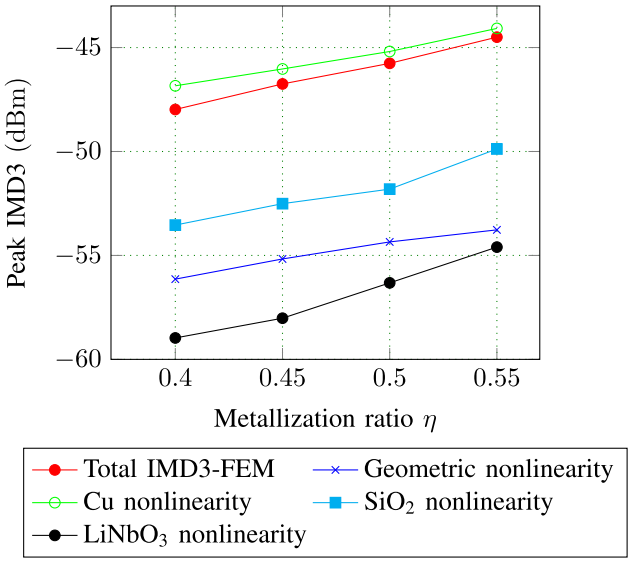

Fig. 9. Simulated magnitude of IMD3 peak power for different nonlinearity combinations and metallization ratios (η).

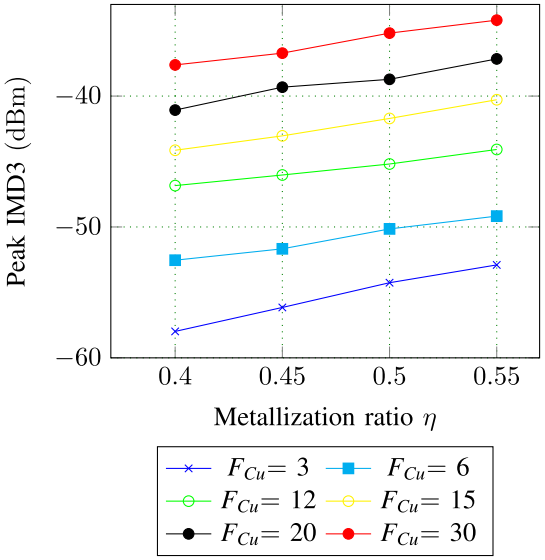

Fig. 10. Simulated magnitude of IMD3 peak power for different scaling factors of Cu metal and metallization ratios (η). Scaling factors of $F_{\mathrm{SiO_2}}$ and $F_{\mathrm{LiNbO_3}}$ are zero.

Cu, SiO_2, and $LiNbO_3$ layers. Obviously, the large scaling factor for the Cu nonlinearity (F_{Cu}) in comparison to the scaling factor of SiO_2 ($F_{\mathrm{SiO_2}}$) and $LiNbO_3$ ($F_{\mathrm{LiNbO_3}}$) favors the dominance of the Cu electrodes in the total IMD3.

The results of calculations for different scaling factors of Cu metal are shown in Fig. 10. In this case, the role of Cu nonlinearity is evaluated while considering the material nonlinearities of the SiO_2 ($F_{\mathrm{SiO_2}}$) and $LiNbO_3$ ($F_{\mathrm{LiNbO_3}}$) as zero. With increasing scaling factor of Cu, the total IMD3 also increases. It should be noted that a large scaling factor of SiO_2 and a small scaling factor of Cu are not giving the same total IMD3-FEM as shown in Fig. 8, confirming that the fitting of $F_{\mathrm{SiO_2}}$ and F_{Cu} with respect to the periodic P-matrix simulation is nonambiguous.

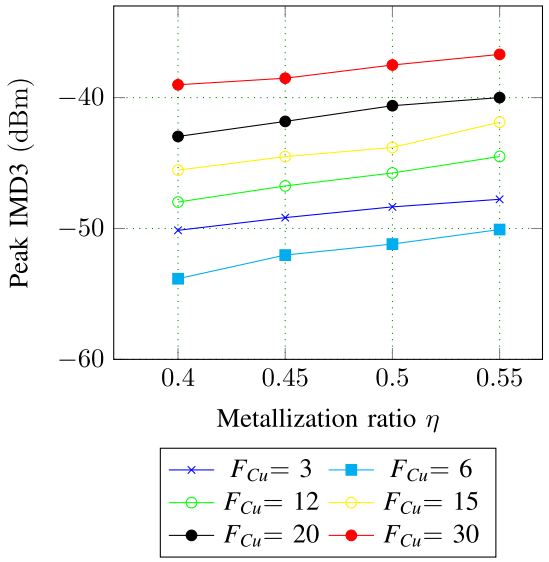

Fig. 11. Simulated magnitude of IMD3 peak power for different scaling factors of Cu metal and metallization ratios (η). The values for the scaling factors of F_{SiO_2} and F_{LiNbO_3} are those of Table II.

In addition, the role of Cu nonlinearity has been investigated by calculations taking into account the material nonlinearities of the SiO_2 (F_{SiO_2}) and $LiNbO_3$ (F_{LiNbO_3}) also as shown in Fig. 11. Except for the case when $F_{Cu} = 3$, the total IMD3 is increased with increasing scaling factors of Cu.

From the overall results of our comparison of the periodic P-matrix simulations with FEM simulations (Fig. 8), using the scaling factors listed in Table II for different η, we are led to the conclusion that the metal electrodes play a dominant role that confirms the results presented earlier [8]. As expected, nonlinear FEM shows that the IMD3 power, calculated with geometric nonlinearity only, is much lower than the total IMD3. Note that the geometric and material nonlinearities contribute to IMD3 in a partly nonadditive way.

C. Direct and Cascaded Nonlinearities

In our calculations of IMD3 at frequency $2f_1 - f_2$ for two input tones with frequencies f_1 and f_2, respectively, we apply the perturbation theory, which yields three contributions as illustrated in Fig. 12. Apart from a contribution due to third-order nonlinearity, being proportional to nonlinear tensor data of up to fourth order [symbolized by C_3 in Fig. 12(b)], there are two contributions resulting from cascaded second-order nonlinearity, depending on nonlinear tensor data of up to third order [symbolized by C_2 in Fig. 12(a) and (c)]. The first of these two parts involves the second harmonic of the input tone f_1, the second involves a low-frequency wave of frequency at $f_1 - f_2$.

The total IMD3 due to the formation of three contributions (directly or indirectly with cascading) is shown in Fig. 13 for the metallization ratio $\eta = 0.55$. The low-frequency contribution is the most significant for the SAW structures under consideration here at around 1 GHz, followed by the second harmonic and direct contributions. Generally, the contributions

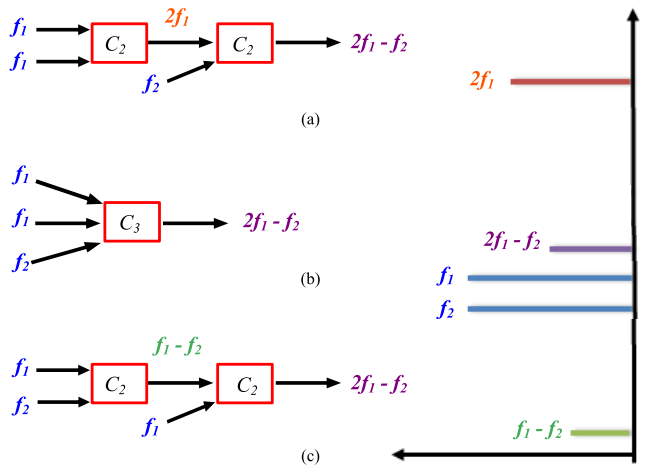

Fig. 12. Schematic representation of different contributions to the total IMD3. (a) Second-harmonic contribution. (b) Direct contribution. (c) Low frequency contribution.

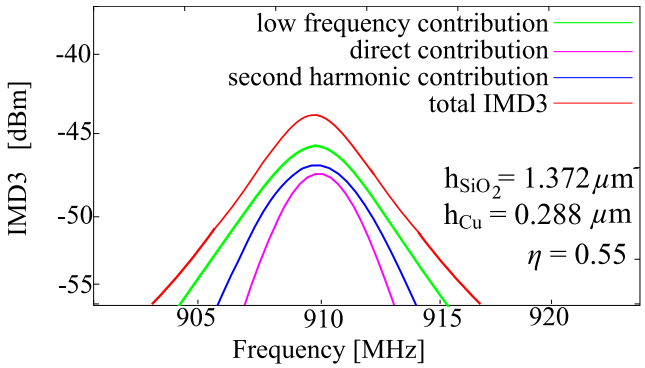

Fig. 13. Direct and cascaded nonlinearities that form the total IMD3 of the S-resonator.

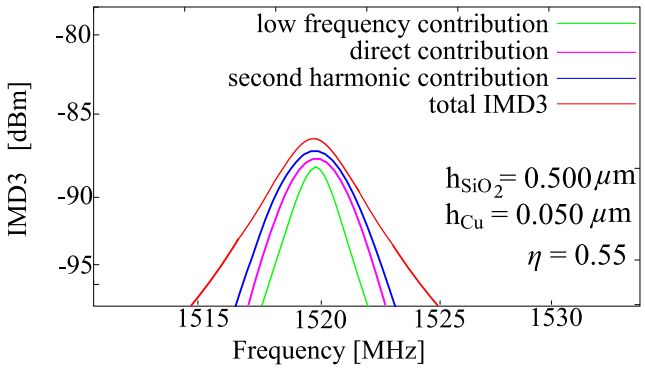

Fig. 14. Direct and cascaded nonlinearities that form the total IMD3 of S-resonator for the case when SiO_2 thickness is reduced from $h_{SiO_2} = 1.372$ μm to $h_{SiO_2} = 0.500$ μm, while the thickness of Cu is reduced from $h_{Cu} = 0.288$ μm to $h_{Cu} = 0.050$ μm.

are of the same order of magnitude and so all of them have to be taken into account.

For different $\eta = 0.40, 0.45, 0.50$, the low-frequency contribution is the most dominant, followed by the second harmonic and direct contributions.

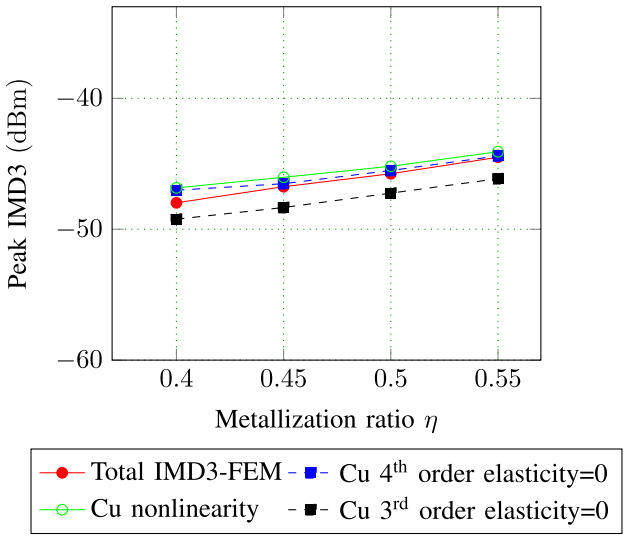

Fig. 15. Simulated magnitude of IMD3 peak power for different nonlinearity conditions and metallization ratios (η) for metal electrode.

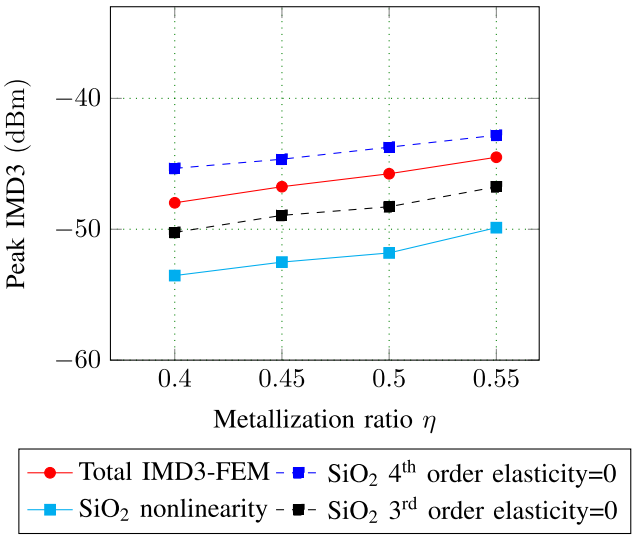

Fig. 16. Simulated magnitude of IMD3 peak power for different nonlinearity conditions and metallization ratio (η) for film oxide.

But when the thickness of SiO_2 (h_{SiO_2}) and Cu (h_{Cu}) are reduced, the second-harmonic (H2) contribution becomes the dominant one, followed by the direct and low-frequency contributions as shown in Fig. 14. This confirms previous reasoning that the H2 contribution is significant in the case of low dispersion [8].

D. Contributions of Higher Order Material Nonlinearities

Figs. 15 and 16 compare the effects of third- and fourth-order elasticity for metal and SiO_2 film. "Cu nonlinearity" in Fig. 15 is calculated while considering the material nonlinearity of SiO_2 (F_{SiO_2}) and $LiNbO_3$ (F_{LiNbO_3}) as zero. Similarly, in Fig. 16, "SiO_2 nonlinearity" is evaluated while considering the material nonlinearity of Cu (F_{Cu}) and $LiNbO_3$ (F_{LiNbO_3}) as zero.

For "Cu fourth-order elasticity = 0," only the fourth-order elastic constants of Cu are kept zero, while the nonlinear tensor data of other materials as well the third-order elastic constants of Cu are not changed. Similarly, for the case "Cu third-order elasticity = 0," subsequently for "SiO_2 third-order elasticity = 0" and "SiO_2 fourth-order elasticity = 0" shown in Fig. 16.

As can be seen in Figs. 15 and 16, when the fourth-order elastic constants of Cu and SiO_2 are kept zero, then the peak IMD3 power is increased compared to the case where the third-order elastic constants of Cu and SiO_2 are kept zero, confirming that IMD3 due to third-order constants is more dominant than IMD3 due to fourth-order elastic constants of the Cu metal electrode and SiO_2. For copper and especially SiO_2, a strong compensation between the third- and fourth-order elastic constants is observed.

Fig. 17 shows the influence of individual third-order nonlinear tensor data of $LiNbO_3$ on the overall calculation of IMD3 in nonlinear FEM. For "$LiNbO_3$ third-order elasticity = 0," only the third-order elastic constants of $LiNbO_3$ are kept zero, while the nonlinear tensor data of other materials as well the third-order dielectric, piezoelectric, and electrostrictive constants of $LiNbO_3$ are not changed and

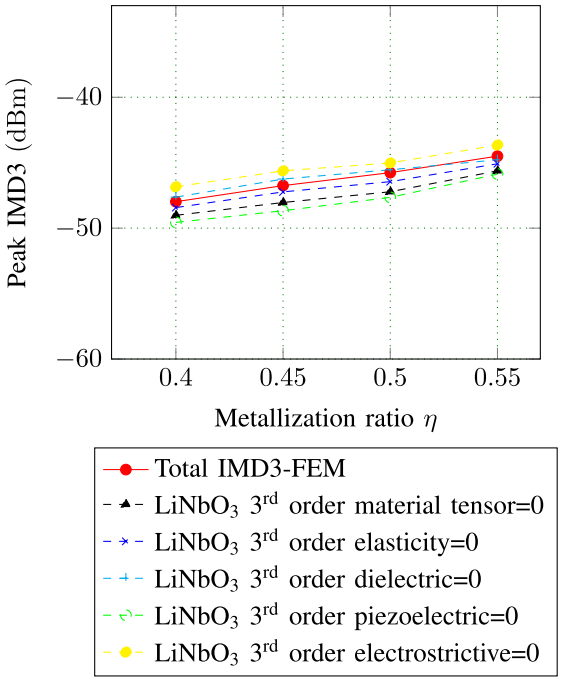

Fig. 17. Simulated magnitude of IMD3 peak power for different nonlinearity conditions and metallization ratio (η) for lithium niobate.

similarly for the other cases. When the third-order nonlinear piezoelectric constants are disabled, the total IMD3 reduced the most, followed by nonlinear elastic constants, nonlinear dielectric, and nonlinear electrostrictive constants. The contribution of nonlinear electrostrictive constants is also significant and plays a role of compensation to the overall nonlinearity.

V. Conclusion

In this paper, a method is described and its viability is demonstrated, which allows for the identification of the role of different kinds of electroacoustic nonlinearities in the SAW devices. This method is based on comparison of measurement

results and nonlinear P-matrix calculations for finite devices and on the comparison between the nonlinear P-matrix and FEM calculations for an infinite periodic system.

With the assumption that the nonlinearity is due to the materials and no other effects, TC-SAW devices with different metallization ratios are investigated. Only two scaling factors for these material nonlinearities have been introduced for the metal and the TC layer, which are 12 and 3, respectively. These scaling factors are sufficient to reproduce all IMD3 measurements quite accurately with the help of FEM simulations.

It is shown that the direct contribution of third-order nonlinearity and the two contributions of cascaded nonlinearity (involving the second harmonic and a low-frequency component) are all significant, and none of them can be neglected. Furthermore, third- and fourth-order nonlinearities seem to partially compensate each other at least in the case of Cu and SiO_2 and that the piezoelectric contribution is the most important one in $LiNbO_3$. The copper metallization is dominating the total IMD3, which is in line with the previous investigations.

Appendix A
IMD3 Current and IMD3 Power Calculation

The nonlinear IMD3's current and power are computed for a resonator measured in reflection as shown in Fig. 18 and both the input tones have the same power levels.

The computation of the IMD3 signal follows in accordance with [3] as the following.

1) Perform linear computations at the input frequencies f_1 and f_2. The relation of current $\mathbf{I}$ and voltage $\mathbf{U}$ is given as

$$\mathbf{I} = y\mathbf{U} \tag{5}$$

where y is the linear admittance. In order to determine the nonlinear current at $f_{\text{imd}} = 2f_1 - f_2$, the voltage at f_1 and f_2 are determined. The ingoing and outgoing electromagnetic power waves $\mathbf{a}$ and $\mathbf{b}$, respectively, are

$$\mathbf{a} = \frac{1}{2\sqrt{Z_0}}\mathbf{U} + \frac{\sqrt{Z_0}}{2}\mathbf{I} \tag{6}$$

and

$$\mathbf{b} = \frac{1}{2\sqrt{Z_0}}\mathbf{U} - \frac{\sqrt{Z_0}}{2}\mathbf{I} \tag{7}$$

where Z_0 is 50 Ω. Inserting (5) into (6) allows to determine the voltage at input frequencies as a function of the applied power wave $\mathbf{a}$

$$\mathbf{U} = \frac{2\sqrt{Z_0}\mathbf{a}}{1 + Z_0 y}. \tag{8}$$

2) Nonlinear current source i_{NL} on the acoustic track at $f_{\text{imd}} = 2f_1 - f_2$ is given as

$$i_{\text{NL}} = y_{\text{IMD3}}(f_1) \cdot \mathbf{U}^2(f_1) \cdot \mathbf{U}^*(f_1 + \Delta f). \tag{9}$$

Here, $f_2 = f_1 + \Delta f$ and y_{IMD3} is the nonlinear admittance. Applying (8) in (9), the nonlinear current

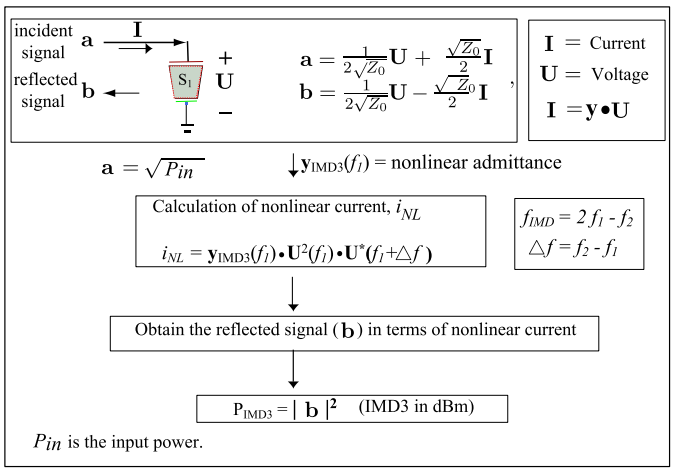

Fig. 18. Calculation of IMD3 power from a reflected signal of series resonator.

can be computed as

$$i_{\text{NL}} = -y_{\text{IMD3}}(f_1) \cdot \frac{8(\sqrt{Z_0})^3(\mathbf{a})^3}{(1 + Z_0 \cdot y(f_1))^2} \cdot \frac{1}{1 + Z_0 \cdot y^*(f_1 + \Delta f)}. \tag{10}$$

3) Now, we compute the reflected outgoing power waves at mixing frequency $f_{\text{imd}} = 2f_1 - f_2$. Fig. 19 shows the flow of current in the nonlinear circuit. At mixing frequency f_{imd}, a current source is connected in parallel to the resonator known as nonlinear current, i_{NL}. The admittance of a resonator is denoted as y.

Recalling Kirchoff's circuit laws, the current is a signed (positive or negative) quantity reflecting direction toward or away from node, using this principle, it can be stated as

$$i_1 + i_2 = 0 \begin{cases} i_1 + i_3 + i_{\text{NL}} = 0 \\ i_2 = i_3 + i_{\text{NL}}. \end{cases} \tag{11}$$

The electric boundary condition is the absence of incoming waves, i.e., $\mathbf{a} = 0$. The potentials at the two ports in Fig. 19 are defined as

$$\mathbf{a} = 0 \begin{cases} \mathbf{U}_1 = -Z_0 \cdot i_1 \\ \mathbf{U}_2 = 0. \end{cases} \tag{12}$$

Using (11) and (12), the current flowing into the resonator, i_3 is calculated as

$$\begin{aligned} i_3 = y \cdot (\mathbf{U}_2 - \mathbf{U}_1) &= -Z_0 \cdot y \cdot (i_1) \\ &= -Z_0 \cdot y \cdot i_2. \end{aligned} \tag{13}$$

From (11) and (13), the total current i_2 is calculated in terms of nonlinear current i_{NL} $(f_1 - \Delta f)$ as

$$i_2 = \frac{i_{\text{NL}}(f_1 - \Delta f)}{1 + Z_0 \cdot y}. \tag{14}$$

Putting (14) into (7), we compute the reflected outgoing power waves at $f_{\text{imd}} = 2f_1 - f_2$ as

$$\mathbf{b} = -\sqrt{Z_0} \cdot \frac{i_{\text{NL}}(f_1 - \Delta f)}{1 + Z_0 \cdot y}. \tag{15}$$

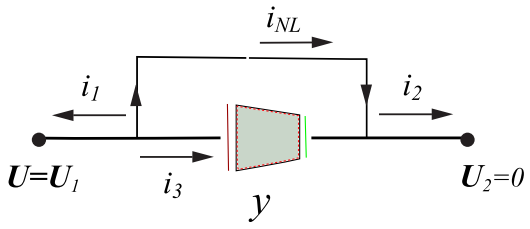

Fig. 19. Flow of current in the nonlinear circuit at $2f_1 - f_2 = f_1 - \Delta f$.

The nonlinear current calculated in (10) is put into (15), and we obtain

$$\mathbf{b} = y_{\text{IMD3}}(f_1) \cdot \frac{8(Z_0)^2(\mathbf{a})^3}{(1 + Z_0 \cdot y(f_1))^2} \cdot \frac{1}{(1 + Z_0 \cdot y^*(f_1 + \Delta f))} \cdot \frac{1}{(1 + Z_0 \cdot y(f_1 - \Delta f))}. \tag{16}$$

Finally, the IMD3 signal in terms of power can be calculated as

$$P_{\text{IMD3}} = |\mathbf{b}^2|. \tag{17}$$

APPENDIX B
NONLINEAR MATERIAL CONSTANTS

The scaling factors are only used for the nonlinear tensor data for the different materials in order to estimate their influence. The linear tensor data will remain unchanged. The meaning of the definitions of the used materials, i.e., the sources of the different tensor data used in the model are mentioned in this section.

The third-order nonlinear constants of lithium niobate are listed in Tables III–VI. The third- and fourth-order elastic constants of copper are mentioned in Tables VII and VIII.

The third and fourth order elastic constants of silicon dioxide are mentioned in Tables IX and X.

TABLE III
THIRD-ORDER ELASTIC CONSTANTS OF LITHIUM NIOBATE [10]

c_{111}	c_{112}	c_{113}	c_{114}	c_{123}
-2120.0	-530.0	-570.0	200.0	-250.0
c_{124}	c_{133}	c_{134}	c_{144}	c_{155}
40.0	-780.0	150.0	-300.0	-670.0
c_{222}	c_{333}	c_{344}	c_{444}	unit
-2330.0	-2960.0	-680.0	-30.0	[GPa]

TABLE IV
THIRD-ORDER PIEZOELECTRIC CONSTANTS OF LITHIUM NIOBATE [10]

e_{115}	e_{222}	e_{125}	e_{126}	e_{135}
17.10	15.00	19.90	-15.90	19.60
e_{136}	e_{145}	e_{311}	e_{312}	e_{313}
-0.90	20.30	14.70	13.00	-10.00
e_{314}	e_{333}	e_{344}	unit	
11.00	-17.30	-10.20	[C/m^2]	

TABLE V
THIRD-ORDER ELECTROSTRICTION CONSTANTS OF LITHIUM NIOBATE [18]

h_{11}	h_{12}	h_{13}	h_{14}	h_{31}
111.00	219.00	232.00	151.00	19.00
h_{33}	h_{41}	h_{44}	unit	
-276.00	185.00	-183.00	10^{-11} [F/m]	

TABLE VI
THIRD-ORDER DIELECTRIC CONSTANTS OF LITHIUM NIOBATE [10]

ϵ_{31}	ϵ_{22}	ϵ_{33}	unit
-2.810	-2.400	-2.910	10^{-19} [F/V]

TABLE VII
THIRD-ORDER ELASTIC CONSTANTS OF COPPER [12]

c_{123}	c_{144}	c_{456}	unit
-6.570	1.720	-3.900	10^2 [GPa]

TABLE VIII
FOURTH-ORDER ELASTIC CONSTANTS OF COPPER [13]

c_{1111}	c_{1112}	c_{1122}	c_{1123}	c_{1144}	c_{2244}
11.936	6.834	6.602	-0.098	0.135	6.628
c_{1244}	c_{2344}	c_{1456}	c_{4444}	c_{4455}	unit
-0.308	5.736	-0.417	5.088	-0.191	10^3 [GPa]

TABLE IX
THIRD-ORDER ELASTIC CONSTANTS OF SILICON DIOXIDE [14]

c_{123}	c_{144}	c_{456}	unit
0.540	0.930	-0.110	10^2 [GPa]

TABLE X
FOURTH-ORDER ELASTIC CONSTANTS OF SILICON DIOXIDE [15]

c_{1111}	c_{1112}	c_{1122}	c_{1123}	unit
11.000	10.800	22.700	8.600	10^3 [GPa]

ACKNOWLEDGMENT

The authors would like to thank Dr. T. Jewula and W. Gawlik for the preparation and measurement of the samples, respectively.

REFERENCES

[1] V. Chauhan *et al.*, "Role of metal electrodes in the generation of third order nonlinearities in TC-SAW devices," in *Proc. IEEE Int. Ultrason. Symp.*, Sep. 2017, pp. 1–4.
[2] A. Mayer *et al.*, "Full 2D-FEM calculations of third-order intermodulations in SAW devices," in *Proc. IEEE Int. Ultrason. Symp.*, Sep. 2016, pp. 1–4.
[3] M. Mayer *et al.*, "Rigorous COM and P-matrix approaches to the simulation of third-order intermodulation distortion and triple beat in SAW filters," in *Proc. IEEE Int. Ultrason. Symp.*, Jul. 2013, pp. 1965–1968.
[4] M. Solal, L. Chen, J. Gratier, and S. Hester, "A nonlinear P matrix model to simulate intermodulation products in SAW devices," in *Proc. IEEE Int. Ultrason. Symp.*, Oct. 2012, pp. 61–66.
[5] S. Inoue *et al.*, "A nonlinear elastic model for predicting triple beat in SAW duplexers," in *Proc. IEEE Int. Ultrason. Symp.*, Oct. 2011, pp. 1837–1841.
[6] R. Nakagawa, T. Suzuki, H. Shimizu, H. Kyoya, and N. Katsuhiro, "A new simulation method for nonlinear characteristics of SAW devices," in *Proc. IEEE Eur. Microw. Integr. Circuit Conf.*, Oct. 2013, pp. 292–295.

[7] L. Chen, M. Solal, J. Briot, S. Hester, D. Malocha, and P. Wahid, "A nonlinear mason model for 3rd order harmonic and intermodulation simulations of SAW duplexers," in *Proc. IEEE Int. Ultrason. Symp.*, Oct. 2012, pp. 56–60.
[8] A. Mayer *et al.*, "Effective nonlinear constants for SAW devices from FEM calculations," in *Proc. IEEE Int. Ultrason. Symp.*, Oct. 2015, pp. 978–981.
[9] R. Nakagawa, T. Suzuki, H. Shimizu, H. Kyoya, and K.-Y. Hashimoto, "Influence of electrode materials and structural design on third-order nonlinear signals of SAW devices," in *Proc. IEEE Int. Ultrason. Symp.*, Sep. 2016, pp. 978–981.
[10] Y. Cho and K. Yamanouchi, "Nonlinear, elastic, piezoelectric, electrostrictive, and dielectric constants of LiNbO," *J. Appl. Phys.*, vol. 61, no. 3, pp. 875–887, 1987.
[11] G. A. Maugin, *Nonlinear Electromechanical Effects and Applications*. Singapore: World scientific, 1985.
[12] A. Seeger and O. Buck, "Die experimentelle Ermittlung der elastischen Konstanten höherer Ordnung," *Zeitschrift Naturforschung A*, vol. 15, no. 12, pp. 1056–1067, 1960.
[13] H. Wang, "Theoretical strength of solids," Ph.D. dissertation, Georgia Inst. Technol., Atlanta, GA, USA, Dec. 2010.
[14] E. H. Bogardus, "Third-order elastic constants of Ge, MgO, and fused SiO_2," *J. Appl. Phys.*, vol. 36, no. 8, pp. 2504–2513, 1965.
[15] K. Kondo, S. Iio, and A. Sawaoka, "Nonlinear pressure dependence of the elastic moduli of fused quartz up to 3 GPa," *J. Appl. Phys.*, vol. 52, no. 4, pp. 2826–2831, 1981.
[16] M. Mayer *et al.*, "Application of a rigorous nonlinear P-matrix method to the simulation of third order intermodulation in test devices and duplexers," in *Proc. IEEE Int. Ultrason. Symp.*, Sep. 2014, pp. 780–787.
[17] R. Nakagawa, T. Suzuki, H. Shimizu, H. Kyoya, T. Kihara, and K. Hashimoto, "Discussion about generation mechanisms of third-order nonlinear signals in surface acoustic wave resonators based on simulation," *Jpn. J. Appl. Phys.*, vol. 43, pp. 98–109, 2016.
[18] A. L. Ganguly and K. L. Davis, "Nonlinear interactions in degenerate surface acoustic wave elastic convolvers," *J. Appl. Phys.*, vol. 51, no. 2, pp. 920–926, 1980.
[19] M. Solal, K. Kokkonen, S. Inoue, J.-B. Briot, B. P. Abbott, and K. J. Gamble, "Observation of nonlinear harmonic generation of bulk modes in SAW devices," *IEEE Trans. Ultrason., Ferroelect., Freq. Control*, vol. 64, no. 9, pp. 1361–1367, Sep. 2017.

Vikrant Chauhan (S'16) was born in Ghaziabad, India, in 1990. He received the M.Sc. degree in electrical engineering from Friedrich Alexander University Erlangen–Nuremberg, Erlangen, Germany, in 2015, where he is currently pursuing the Ph.D. degree with the Institute for Electronics Engineering.

His research interests include bulk acoustic wave (BAW) physics, nonlinear modeling of BAW and surface acoustic wave devices, and RF front ends power amplifier module designs.

Mr. Chauhan is a Student Member of Springer. He was a recipient of the Student Paper Award at the IEEE Asia Pacific Microwave Conference 2016, the finalist and winner of the Student Paper Award at the IEEE International Ultrasonic Symposium 2016 and 2017, respectively, and the IEEE Microwave Theory and Techniques Society Graduate Fellowship in 2018.

Markus Mayer (M'06) was born in Cologne, Germany, in 1968. He received the Diploma degree in physics and the Ph.D. degree in theoretical chemistry from the Technical University of Munich, Munich, Germany, in 1995 and 2000, respectively. His thesis was about simulation of relativistic effects in heavy element chemistry.

In 1999, he joined EPCOS AG (now RF360 Europe GmbH), a Qualcomm–TDK joint venture, Munich, Germany, where he is developing simulation models for surface acoustic wave devices, in particular describing nonlinear effects.

Dr. Mayer has been a member of the IEEE UFFC Society since 2007.

Elena Mayer received the Diploma degree in physics from Lomonosov Moscow State University, Moscow, Russia, in 1983, and the Ph.D. (Kandidat Nauk) degree from the Institute of Radio engineering and Electronics (IRE), Russian Academy of Sciences, Moscow, in 1994.

In 1983, she became an Engineer and subsequently a Scientist with IRE, Russian Academy of Sciences, where her main research topics were surface acoustic waves and their application in electroacoustic devices. In 1998, she joined Siemens Matsushita, Munich, Germany, and subsequently EPCOS AG, Munich, as a Development Engineer, where she was involved in problems related to the modeling and design of surface acoustic wave (SAW) devices. From 2005 to 2012, she was a Scientific Staff Member with the Department of Microsystems, University of Freiburg, Breisgau, Germany, where her research work included high-temperature applications of SAWs. In 2012, she was a Research Fellow with the HS Offenburg University of Applied Sciences, Offenburg, Germany. Her current research activities are investigations of material properties by laser ultrasound and modeling of nonlinearity in SAW devices.

Werner Ruile received the Dipl.Phys. degree from the Ludwig Maximilians University of Munich, Munich, Germany, in 1984, and the Dr.Ing. degree from the Technical University of Munich, Munich, in 1994.

From 1983 to 2000, he was with the Corporate Research and Development, Siemens AG, Munich, where he developed the simulation tools for surface acoustic wave (SAW) devices based on the P-Matrix. In 2000, he joined EPCOS AG, Munich, which is a Group Company of TDK Corporation since 2008, where he was involved in the SAW research and development activities. Since 2017, he has been with RF360 Europe GmbH, Munich, a Qualcomm–TDK joint venture, where he is involved in power durability, loss reduction, temperature compensation, and trimming techniques. He currently focuses on nonlinearities in SAW filters.

Thomas Ebner was born in Ulm, Germany, in 1966. He received the Dipl.-Phys. and Dr.rer.nat. degrees from the University of Ulm, Ulm, in 1995 and 2000, respectively.

In 1999, he joined the Surface Acoustic Wave (SAW) Research and Development Group, EPCOS AG, Munich, Germany, which is a group company of TDK Corporation since 2008 and has been operating under the name RF360 Europe GmbH, Munich, as a Qualcomm–TDK joint venture since 2017, where he was involved in acoustic simulation and reduction of radiation losses of SAW devices. He is currently the Head of the Acoustic Group, Advanced Development Department for Discrete Components, RF360 Europe GmbH.

Ingo Bleyl (M'15) was born in Kulmbach, Germany, in 1968. He received the Diploma degree in experimental physics and the Ph.D. degree from the University of Bayreuth, Bayreuth, Germany, in 1995 and 1998, respectively.

In 1999, he joined the Systems, Acoustics, Waves Business Group, EPCOS AG, Munich, Germany (now RF360 Europe GmbH), a Qualcomm–TDK joint venture, where he was involved in material research and development of surface acoustic wave devices.

Dr. Bleyl has been a member of the IEEE UFFC Society since 2015.

Karl C. Wagner (S'87–M'87) received the Diploma degree in electrical engineering and the Ph.D. degree in technical sciences from the Vienna University of Technology, Vienna, Austria.

He is currently the Head of the Advanced Development Department for Discrete Components, RF360 Europe GmbH, Munich, Germany. He has more than 20 years of experience in the development of microacoustic components and in managing research and development projects. His field of research includes especially the simulation of acoustic, electromagnetic, thermal and coupled fields in electronic components, as well as the design of surface acoustic wave components for wireless communication systems.

Dr. Wagner is an Active Member of the IEEE UFFC and MTT Societies and currently serves as a TPC Group Co-Chair of IUS.

Robert Weigel (S'88–M'89–SM'95–F'02) was born in Ebermannstadt, Germany, in 1956. He received the Dr.-Ing. and Dr.-Ing.habil. degrees in electrical engineering and computer science from the Munich University of Technology, Munich, Germany.

From 1994 to 1995, he was a Guest Professor of surface acoustic wave technology, Vienna University of Technology, Vienna, Austria. He was a Research Engineer, a Senior Research Engineer, and a Professor of RF circuits and systems with the Munich University of Technology until 1996. From 1996 to 2002, he was the Director of the Institute for Communications and Information Engineering, Johannes Kepler University of Linz, Linz, Austria, where he became a Co-Founder of the company DICE in 1999, meanwhile split into an Infineon Technologies (DICE) and an Intel (DMCE) company which are devoted to the design of RFICs and MMICs. In 2000, he was a Professor of RF engineering with Tongji University, Shanghai, China. Since 2002, he has been a Head of the Institute for Electronics Engineering, Friedrich Alexander University Erlangen–Nuremberg, Erlangen, Germany, where he became the Co-Founder of the companies eesy-id and eesy-ic in 2009 and 2012, respectively. He has been engaged in research and development of microwave theory and techniques, electronic circuits and systems, and communication and sensing systems. He has authored or co-authored more than 900 papers in these fields.

Dr. Weigel is an Elected Member of the German National Academy of Science and Engineering, and the Senate of the German Research Foundation. He has been serving on numerous advisory boards of government bodies, research institutes and companies in Europe and Asia as well as on various editorial boards such as that of the PROCEEDINGS OF THE IEEE. He has been a member of numerous conference steering and technical program committees and was Technical Program Chair of several conferences such as the 2002 IEEE International Ultrasonics Symposium in Munich, as well as the General Chair of several conferences such as the 2013 European Microwave Week in Nuremberg, Germany. He has been the Founding Chair of the Austrian coupling of modes/MTT Joint Chapter, Region 8 MTT-S Coordinator, Distinguished Microwave Lecturer, MTT-S AdCom Member, and the 2014 MTT-S President. He was a recipient of the 2007 IEEE Microwave Applications Award. He served in many roles for the IEEE MTT and UFFC Societies. He has also been the Founding Editor of the *Proceedings of the European Microwave Association* in 2008, which then became EuMA's *International Journal of Microwave and Wireless Technologies*.

Andreas P. Mayer (M'94) received the Dipl.-Phys. and Dr.rer.nat. degrees from the University of Münster, Münster, Germany, in 1983 and 1985, respectively.

After research work at the universities of Münster, Perugia, Edinburgh, and UC Irvine on lattice dynamics, surface physics, and nonlinear optics, he was an Assistant and Privatdozent with the Physics Department, University of Regensburg, Regensburg, Germany, from 1991 to 2001. In 2002, he was a Development Engineer with Siemens VDO. In 2008, he became a Professor with HS Offenburg University of Applied Sciences, Offenburg, Germany. His main research interests are in microacoustics, especially nonlinear effects on wave propagation.

Amelie Hagelauer (S'08–M'10) received the Dipl.-Ing. degree in mechatronics and the Dr.-Ing. degree in electrical engineering from the Friedrich Alexander University Erlangen-Nuremberg, Erlangen, Germany, in 2007 and 2013, respectively.

In 2007, she joined the Institute for Electronics Engineering, Friedrich Alexander University Erlangen-Nuremberg, where she was working on thin-film bulk acoustic wave (BAW) filters. Since 2013, she has been focusing on surface acoustic wave/BAW and RF MEMS components, as well as integrated circuits for front ends up to 180 GHz. Since 2016, she has been leading a research group on electronic circuits. She is continuously contributing to the development of RF acoustic community by organizing workshops and student design competitions.

Dr. Hagelauer has been the Chair of MTT-2 Microwave Acoustics since 2015. He served as a Guest Editor for a special issue of the IEEE MTT TRANSACTIONS on the topic of RF Frontends for Mobile Radio, as well as for a special issue in the *MDPI Journal Sensors* on the topic of Surface Acoustic Wave and Bulk Acoustic Wave Sensors.